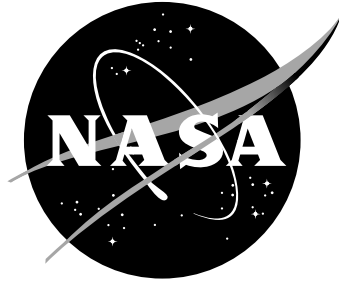


NASA Technical Memorandum 112856



Reentry-F Flowfield Solutions at 80,000 ft.

W. A. Wood, C. J. Riley, and F. M. Cheatwood
Langley Research Center, Hampton, Virginia

May 1997

National Aeronautics and
Space Administration
Langley Research Center
Hampton, Virginia 23681-0001

Reentry-F Flowfield Solutions at 80,000 ft.

William A. Wood*, Christopher J. Riley† and F. McNeil Cheatwood‡

NASA Langley Research Center, Hampton, VA 23681

Three equilibrium-air numerical solutions are presented for the Reentry-F flight-test vehicle at Mach 20, 80,000 ft. conditions, including turbulent flow predictions. The three solutions are from a thin-layer Navier-Stokes code, coupled thin-layer and parabolized Navier-Stokes codes, and an approximate viscous shock-layer code. Boundary-layer and shock-layer profiles are presented and compared between the three solutions, revealing close agreement between the three solution methods. Notable exceptions to the close agreement, with 7–10 percent discrepancies, occur in the density profiles at the boundary-layer edge, in the boundary-layer velocity profiles, and in the shock-layer profiles in regions influenced by the nose bluntness.

Nomenclature

c	Sound speed, m/s
M	Mach number
P	Pressure, Pa
Re_s	Reynolds number based on length s
T	Temperature, K
V	Velocity, m/s
x, y, z	Cartesian body axes, m
α	Angle of attack, deg
η	Wall-normal distance, m
ρ	Density, kg/m ³

Subscripts:

n	Normal
t	Tangential
$tran$	Transition
w	Wall
∞	Freestream

Introduction

REENTRY-F¹ was a flight test conducted in 1968 to study the turbulent reentry environment. The reentry vehicle itself consisted of an instrumented 5-deg half-angle cone, 3.66 m (12 ft.) in length.

The 25 years since the original test have seen a tremendous advancement in the computational resources available for data analysis. The present study seeks to revisit the issues raised by the Reentry-F flight with regards to hypersonic laminar-to-turbulent transition by providing high-fidelity complete-flowfield solutions about the vehicle. These flowfield solutions can then provide a basis for the development of improved transition prediction and modeling methods.

The application of such improved transition and turbulence prediction methods would be of significant benefit to the X-33 and X-34 reusable-launch-

vehicle programs. Current analysis techniques for hypersonic turbulent flow have appreciable aerodynamic and aerothermal uncertainties, and improved prediction methods would lower the costs associated with over-designing the vehicles to compensate for the prediction uncertainties.

Codes

Three algorithms, each representing a different level of physical modeling, were used to generate the flowfield solutions in the present study.

The Langley Aerothermodynamic Upwind Relaxation Algorithm (LAURA)² is a finite-volume, shock-capturing algorithm with second-order spatial accuracy for the steady-state solution of viscous or inviscid hypersonic flows. The scheme employs a point implicit relaxation strategy with upwind-biased flux-difference splitting for perfect gas, equilibrium air, or nonequilibrium air calculations. In the present study LAURA solved the thin-layer Navier-Stokes (TLNS) equations for laminar and Farve-averaged flows.³

Solving the TLNS equations is time and memory intensive, iterating globally on the domain in a time-marching fashion. However, this is a robust approach that is good for handling flowfields with subsonic regions.

LAURA was also employed in conjunction with the Upwind Parabolized Navier-Stokes Solver (UPS).⁴ The procedure of Wood^{5–8} was used whereby the flowfield about the spherically-blunted nose (3.43 mm radius) was solved with LAURA while the 4 m conical body was solved with UPS. UPS is an upwind, finite-volume, parabolized Navier-Stokes (PNS) code with perfect gas, equilibrium air, and chemical nonequilibrium capability. It is second-order accurate in the crossflow plane and first order accurate in the marching direction, and contains a Baldwin-Lomax⁹ algebraic turbulence option.

The PNS equations are cast as a space-marching scheme, solving the entire domain in a single stream-wise sweep. This is contrasted with a TLNS algorithm which typically iterates hundreds or thousands of times

*Aerospace Technologist, Aerothermodynamics Branch, Aero- and Gas-Dynamics Division.

†Aerospace Technologist, Aerothermodynamics Branch, Aero- and Gas-Dynamics Division.

‡Aerospace Technologist, Vehicle Analysis Branch, Space Systems & Concepts Division. Member AIAA.

on the domain. However, PNS algorithms are limited to fully supersonic flows, with the exception of the boundary layer which must be treated specially in most PNS formulations. UPS uses the method of Vigneron¹⁰ to stabilize the subsonic portion of the boundary layer.

Since Reentry-F is modeled with a spherical nose in the present study, the PNS code cannot be utilized upstream of the sonic line. This is why LAURA is needed to solve the nose region before UPS can march the solution down the conical portion of the vehicle.

The third code utilized was the Approximate Viscous Shock-Layer (AVSL)¹¹ algorithm. AVSL is an approximate viscous shock-layer technique whose governing equations are identical to those of the standard viscous shock-layer technique except that Maslen's pressure relation¹² is substituted for the normal momentum equation. The streamwise momentum equation remains unchanged.

AVSL is a shock-fitting inverse method, iterating on the bow-shock shape to match the desired surface shape for that portion of the shock layer encompassed by the sonic line. Downstream of the sonic line the solution is space-marched in a manner similar to the PNS treatment, and hence requires a supersonic shock layer downstream of the nose. Being shock-fitting, AVSL is not appropriate to flowfields with internal shocks, whereas both UPS and LAURA, being shock-capturing, can model the internal shocks in addition to the bow shock.

Cases

Three cases are considered, corresponding to the three sets of governing equations solved by the LAURA, UPS, and AVSL computer codes. All of the solutions simulate the trajectory point at an altitude of 24.38 km (80,000 ft.).

Case A is the three-dimensional combined LAURA-UPS solution. The angle of attack is 0.14 deg. Both LAURA and UPS were run using the equilibrium air model of Srinivasan, Tannehill, and Weilmuenster.¹³ The UPS solution was begun at 3.55 mm and extended beyond the full vehicle length to 4 m. Transition was specified to commence at 2 m, in approximate agreement with the flight data, giving $Re_s = 36.9 \times 10^6$ based on surface length from the nose. The wall temperature was held constant at 467.9 K. Table 1 lists the freestream conditions for Case A along with Cases B and C. The computational mesh contained 101 points normal to the body surface and 15 points in the circumferential direction around half the vehicle. Only the port side of the vehicle was included in the computational domain since there was zero side-slip. The final streamwise step-size for the UPS portion of the solution was 5 mm.

Case B is an axisymmetric LAURA solution. In this case the equilibrium air model of Liu and Vinokur¹⁴

Table 1 Reentry-F freestream conditions.

	Case A	Case B	Case C
M_∞	19.97	19.97	19.97
α	0.14	0	0
ρ_∞	0.04479	0.446	0.04480
T_∞	221.3	221	221.3
T_w	467.94	variable	467.94
P_∞	2830.9	2843.5	2844.6
V_∞	5936.4	5966	5954.2
c_∞	297.3	298.7	298.2
x_{end}	4.036	3.683	4.036
x_{tran}	2.012	2.0	2.012

Table 2 T_w variation for Case B.

x	T_w
0	1453
0.053	1194
0.078	1065
0.130	806
0.257	667
0.792	513
1.328	462
1.864	437
2.527	427
3.086	486
3.673	542

was used along with the Cebici-Smith¹⁵ algebraic turbulence model. As in Case A, transition was specified to begin at 2 m. The wall temperature varied along the length of the vehicle according to the measured flight data with a maximum of 1450 K at the nose and a minimum of 427 K located just past the onset of transition. A tabulation of the imposed wall temperature versus axial distance for Case B is contained in Table 2. The axisymmetric grid contained 201 points in the streamwise direction and 97 points normal to the body.

Case C is an axisymmetric AVSL solution. The equilibrium air model used is due to Hansen.¹⁶ The Cebici-Smith turbulence model is employed with AVSL and the transition region is modeled after Dhawan and Narashima.¹⁷ This is the same transition method as is used in both UPS and LAURA. The wall temperature was held constant at the same value as for Case A. The grid for this case contained 101 points normal to the body.

Results

Results will be presented in the form of profile plots taken from the windside and leeside centerlines of Case A, the three-dimensional case, and the corresponding points from Cases B and C, the axisymmetric

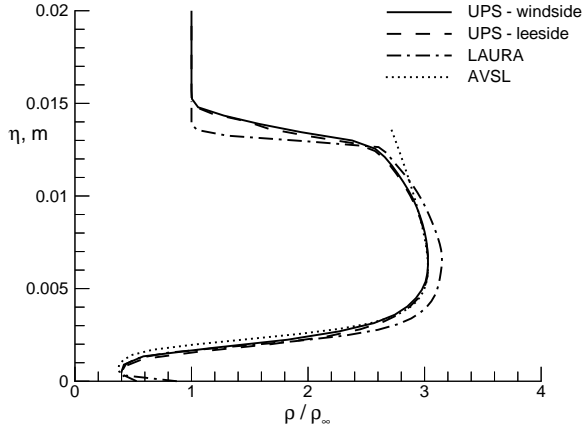


Fig. 1 Shock-layer density profiles, $x = 0.5$ m.

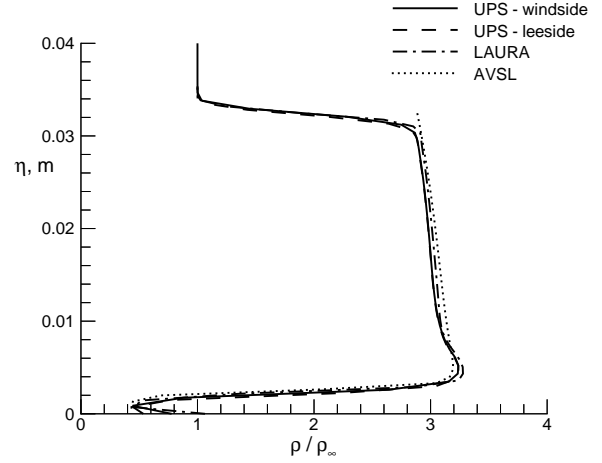


Fig. 3 Shock-layer density profiles, $x = 1.5$ m.

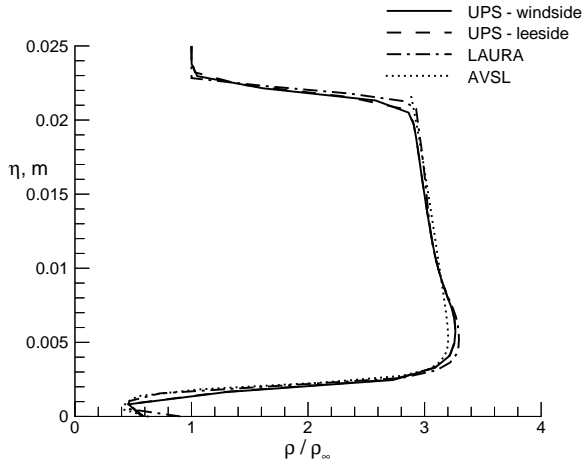


Fig. 2 Shock-layer density profiles, $x = 1.0$ m.

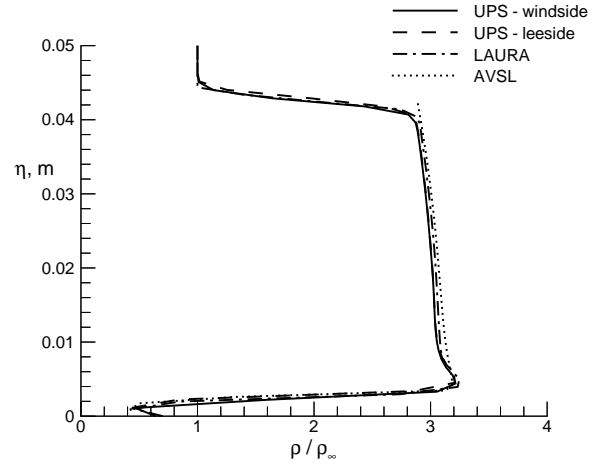


Fig. 4 Shock-layer density profiles, $x = 2.0$ m.

cases. Both shock-layer and boundary-layer profiles are displayed versus the body-normal distance from the surface. The profiles presented are for density, ρ/ρ_∞ , surface-tangential velocity component, V_t/c_∞ , surface-normal velocity component, V_n/c_∞ , and pressure, P/P_∞ . Profiles are extracted at five axial locations, $x = 0.5, 1.0, 1.5, 2.0$, and 4.0 m.

Density profiles

Shock-layer density profiles are plotted in Figs. 1–5 at the five axial data stations. Figure 5 plots only the results of Cases A and C at $x = 4$ m, because Case B, the LAURA solution, had been terminated prior to this station. The profiles from Cases A and B extend beyond the shock layer into the freestream because both UPS and LAURA are shock-capturing codes. The results of Case C stop at the shock because AVSL is a shock-fitting code, obtaining post-shock conditions analytically from the Rankine-Hugoniot relations.

Figure 1 shows the bow shock is better resolved at the most upstream location, $x = 0.5$ m, by the LAURA solution than the UPS result. This is attributed to a

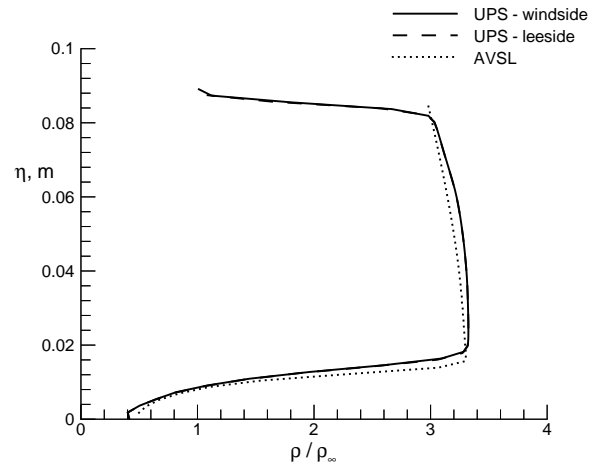


Fig. 5 Shock-layer density profiles, $x = 4.0$ m.

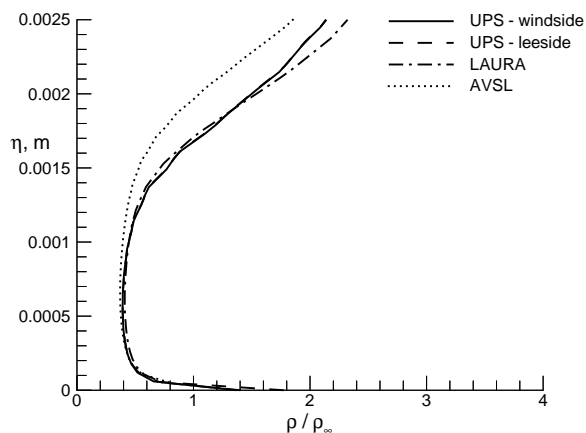


Fig. 6 Boundary-layer density profiles, $x = 0.5$ m.

tighter grid-spacing normal to the shock in the Case B versus Case A grid. Figures 2–4 show comparable shock-resolution between LAURA and UPS, where the grids are more similar than at $x = 0.5$ m.

In Fig. 1 the shock-layer is still strongly influenced by the nose bluntness, as the density profile outside the boundary layer is continuously curved. Progressing downstream in Figures 2–5 the shock-layer assumes a more conical-flow profile, becoming nearly linear outside the boundary layer. However, a “bubble” in the density profile does persist between the boundary layer and the conical-flow profile downstream to the last laminar station, Fig. 4. This “bubble” persisting since the nose is swallowed by the turbulent boundary layer, Fig. 5.

Comparing the performance of the three codes, LAURA predicts higher densities by 7 percent than either UPS or AVSL, which agree closely with each other, at $x = 0.5$ m in Fig. 1. In all figures the wind-side and leeside results of Case A are very similar, which is not unexpected since the angle of attack is only 0.14 deg. The UPS and LAURA profiles overplot in Figs. 2–4. The AVSL solution matches the UPS and LAURA profiles except that the “bubble” above the boundary layer is lost by $x = 1$ m, seen in Figs. 2–4. The turbulent profile in Fig. 5 shows a 3-percent difference in density between the UPS and AVSL solutions.

Boundary-layer density profiles are charted in Figs. 6–10, following the same sequence as Figs. 1–5. At the furthest upstream station, $x = 0.5$ m, Fig. 6, excellent agreement through the boundary layer is seen between the Case A UPS solution and the Case B LAURA result. At the boundary-layer edge the UPS and LAURA solutions separate, establishing the different shock-layer profiles seen in Fig. 1. The Case C AVSL solution has excellent agreement throughout two-thirds of the boundary layer, but does not recover the density to the shock-layer value as soon as UPS and LAURA predict. The AVSL densities over-state

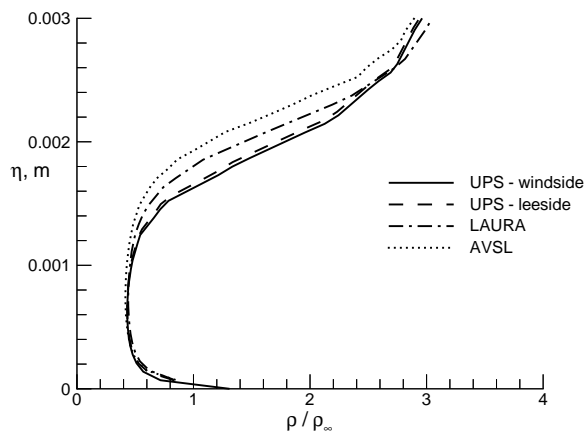


Fig. 7 Boundary-layer density profiles, $x = 1.0$ m.

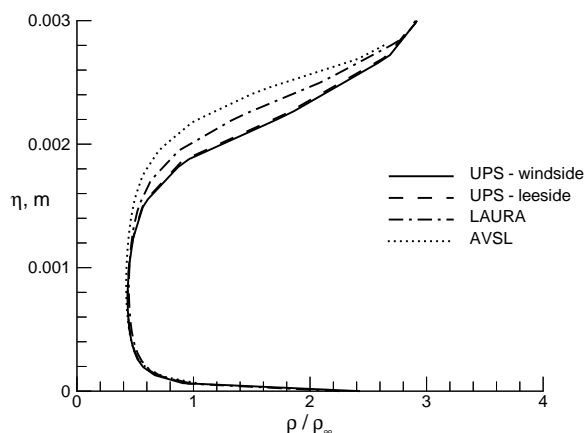


Fig. 8 Boundary-layer density profiles, $x = 1.5$ m.

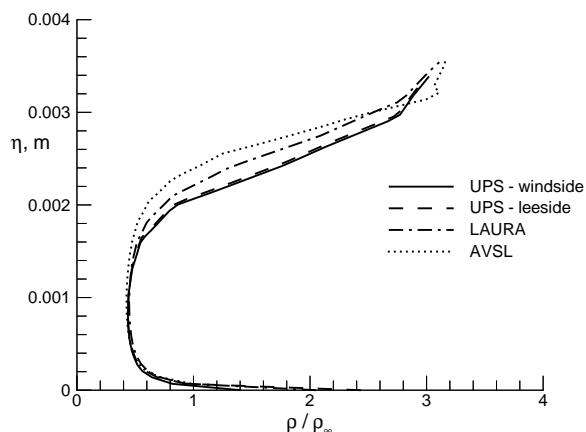


Fig. 9 Boundary-layer density profiles, $x = 2.0$ m.

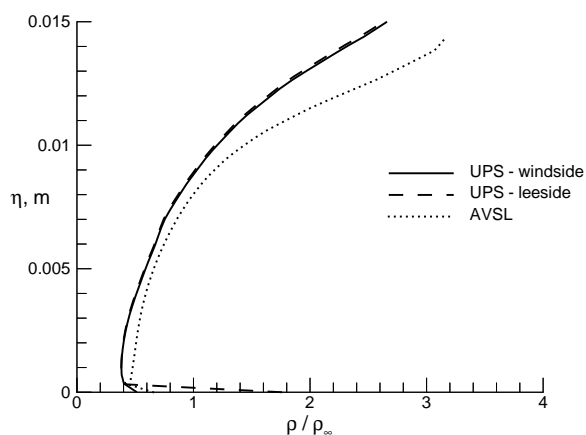


Fig. 10 Boundary-layer density profiles, $x = 4.0$ m.

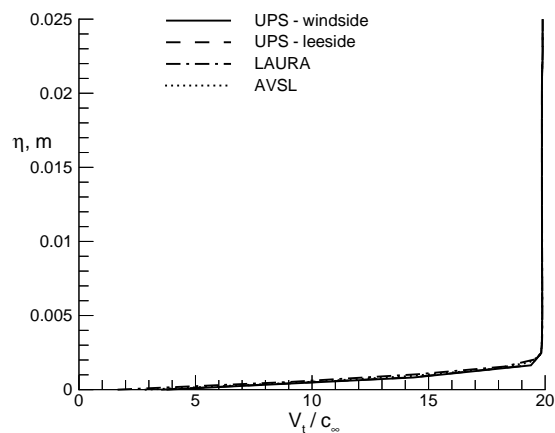


Fig. 12 Shock-layer tangential-velocity profile, $x = 1.0$ m.

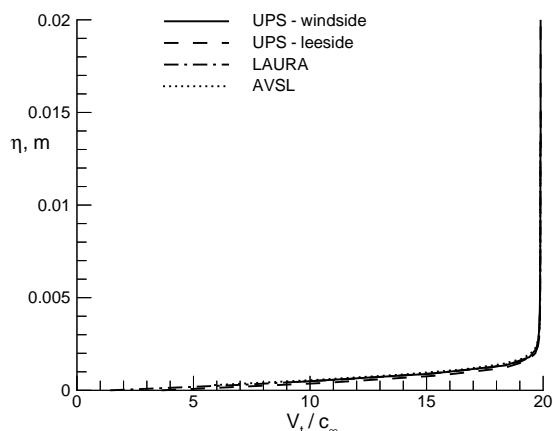


Fig. 11 Shock-layer tangential-velocity profile, $x = 0.5$ m.

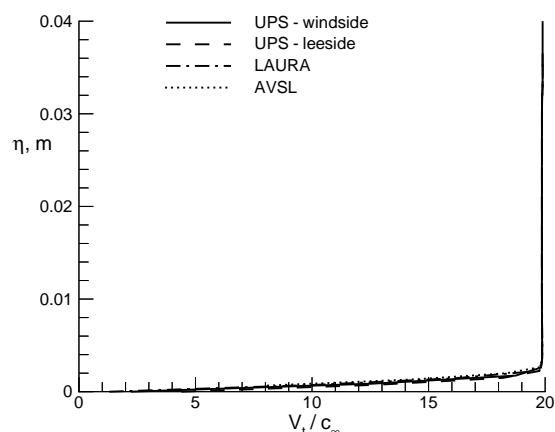


Fig. 13 Shock-layer tangential-velocity profile, $x = 1.5$ m.

the influence of the boundary layer by 15 percent, a trend repeated in Figs. 7–9.

Density profiles at the remaining laminar stations, Figs. 7–9, show excellent agreement between the three cases out to the boundary-layer edge, where the LAURA edge profile is sandwiched by the UPS edge profile below and the AVSL profile above. The three cases converge to similar shock-layer values outside the boundary-layer edge region.

At the turbulent station, Fig. 10, the AVSL solution predicts up to 10 percent higher densities than UPS through the boundary layer and up to the boundary-layer edge, where the differences are larger.

Tangential-velocity profiles

Shock-layer profiles for the velocity component tangential to the cone surface, in the streamwise direction, are plotted in Figs. 11–15. These figures show excellent agreement between all three solution methods through the shock layer. This agreement contrasts somewhat with the differences noted in the shock-layer density

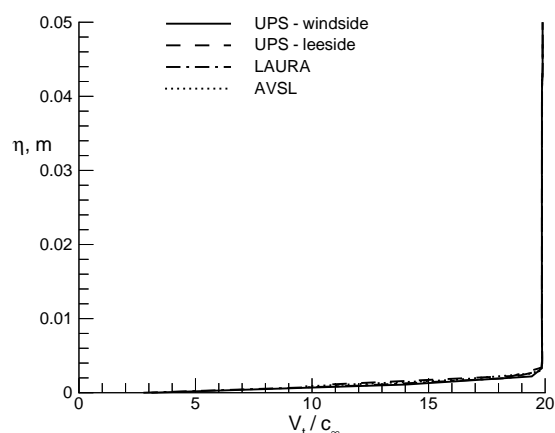


Fig. 14 Shock-layer tangential-velocity profile, $x = 2.0$ m.

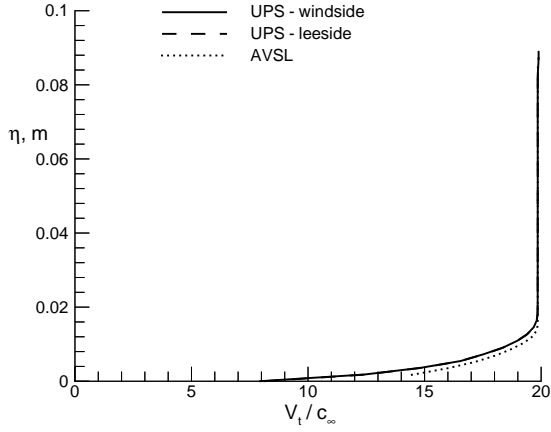


Fig. 15 Shock-layer tangential-velocity profile, $x = 4.0$ m.

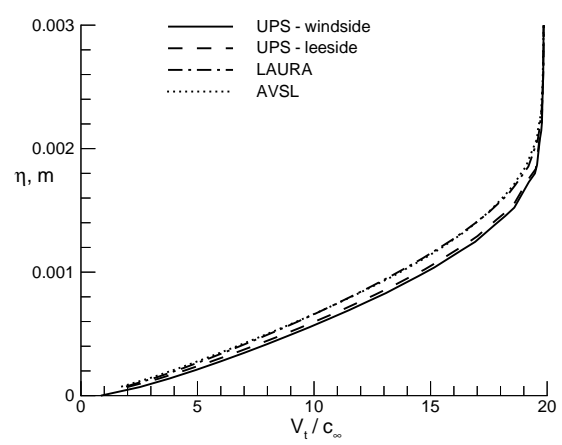


Fig. 17 Boundary-layer tangential-velocity profile, $x = 1.0$ m.

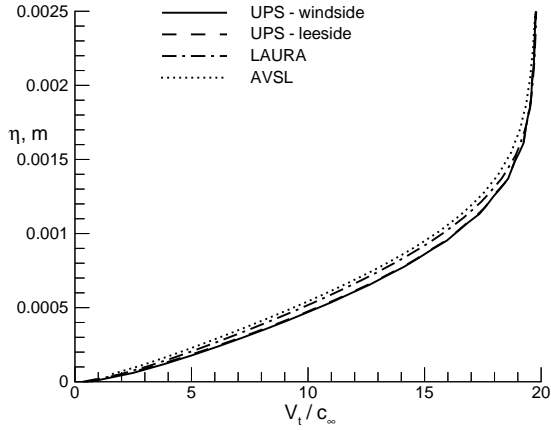


Fig. 16 Boundary-layer tangential-velocity profile, $x = 0.5$ m.

profiles. The densities are more sensitive than the velocities to the differing equilibrium chemistry models in the three codes and to predicted temperature variations throughout the shock layers.

Boundary-layer profiles of the tangential velocity are presented in Figs. 16–20, revealing a noticeable difference between the UPS solution and the LAURA and AVSL solutions. At each of the four laminar stations, Figs. 16–19, UPS predicts a thinner boundary layer, by 10 percent at $x = 2.0$ m, with a fuller profile throughout the boundary layer. This contrasts somewhat with the density boundary-layer profiles in Figs. 6–9 where the densities for all three cases were similar through the majority of the boundary layer, differing only in the edge location.

Examining more closely as a typical location the $x = 1.5$ m station, Fig. 18, UPS predicts a 7 percent increase in tangential velocity through the outer two-thirds of the boundary layer, relative to either the Case B or Case C results. The three solution sets converge at the boundary-layer edge and at the wall,

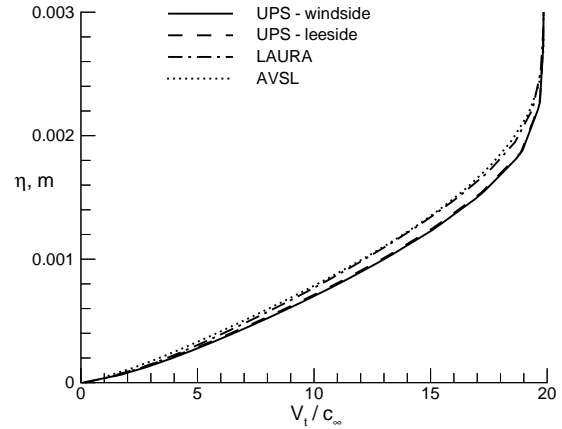


Fig. 18 Boundary-layer tangential-velocity profile, $x = 1.5$ m.

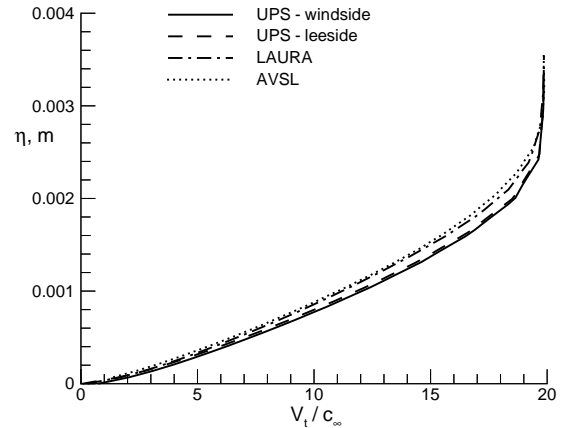


Fig. 19 Boundary-layer tangential-velocity profile, $x = 2.0$ m.

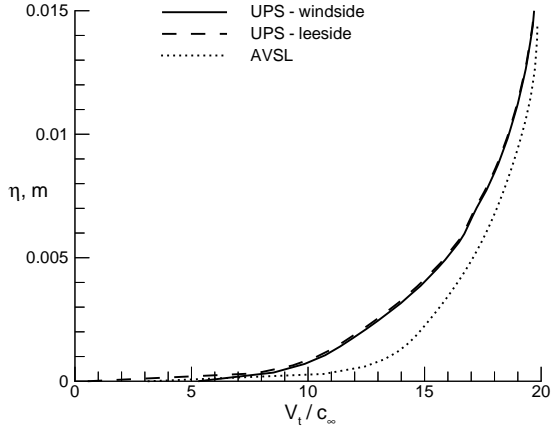


Fig. 20 Boundary-layer tangential-velocity profile, $x = 4.0$ m.

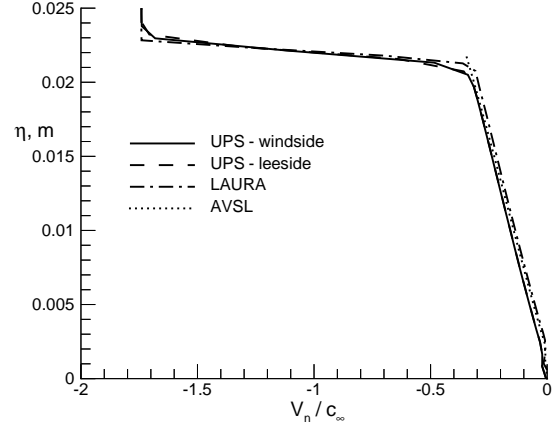


Fig. 22 Shock-layer normal-velocity profile, $x = 1.0$ m.

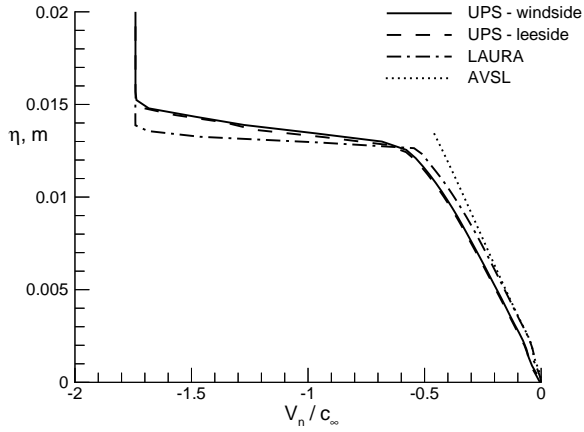


Fig. 21 Shock-layer normal-velocity profile, $x = 0.5$ m.

where the no-slip condition constrains all of the solutions. Differences in the implementation of the equilibrium thermal-property models in the three codes could be contributing to the different velocity gradients through the boundary layer, with a decrease in viscosity corresponding to an increase in tangential-velocity gradient.

The turbulent tangential-velocity profiles, Fig. 20, differ between UPS and AVSL. The AVSL profiles is much fuller than the UPS profile, though the boundary-layer edge predictions are similar.

Normal-velocity profiles

Shock-layer profiles of the velocity component normal to the vehicle surface are presented in Figs. 21–25. The shock-layer values of V_n are negative, indicating flow toward the vehicle surface. A linear variation in V_n is seen through the shock layer, consistent with conical flow.

Figure 21, the furthest upstream location, shows a slight variation in the AVSL solution from the LAURA

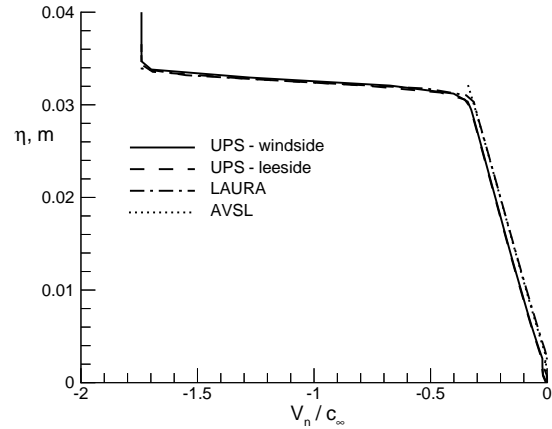


Fig. 23 Shock-layer normal-velocity profile, $x = 1.5$ m.

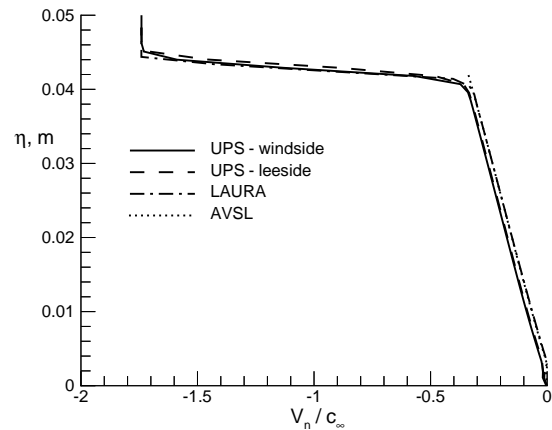


Fig. 24 Shock-layer normal-velocity profile, $x = 2.0$ m.

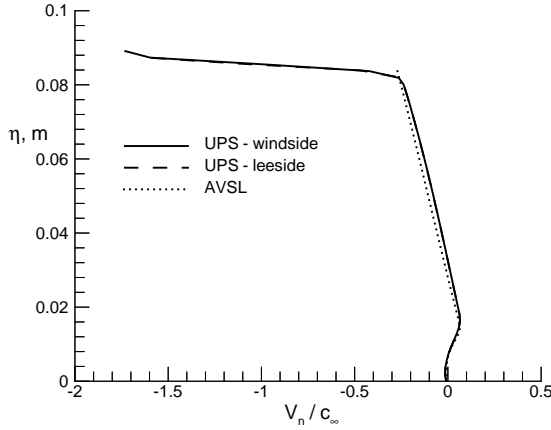


Fig. 25 Shock-layer normal-velocity profile, $x = 4.0$ m.

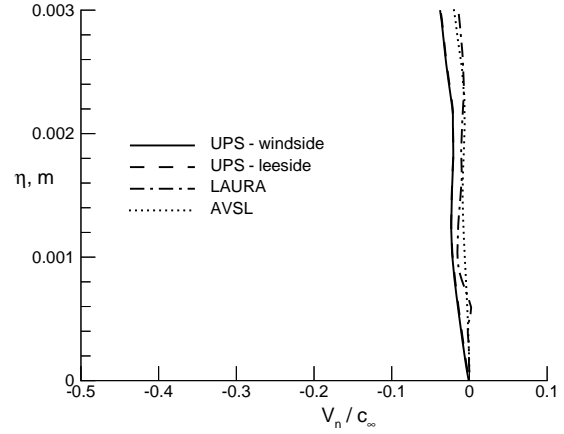


Fig. 27 Boundary-layer normal-velocity profile, $x = 1.0$ m.

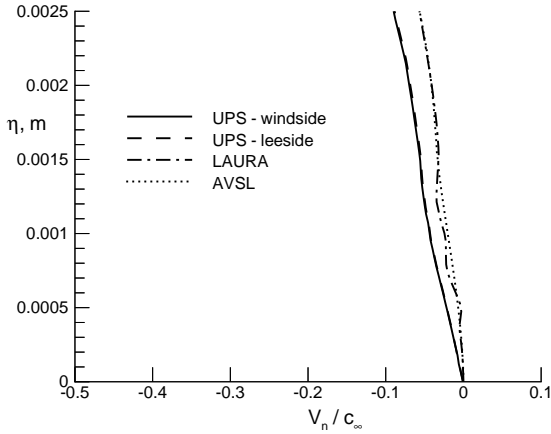


Fig. 26 Boundary-layer normal-velocity profile, $x = 0.5$ m.

results near the shock. Excellent agreement between LAURA and AVSL is seen at three remaining laminar stations, Figs. 22–24.

A very slight, yet discernible, difference can be seen between the UPS and LAURA profiles in Figs. 21–24. Both Case A and B results show the same slope of V_n vs η , but UPS predicts slightly larger magnitudes of the normal-velocity component at a given height above the surface.

At the turbulent station, Fig. 25, the normal velocity is positive near the surface, due to the rapidly thickening displacement thickness in the turbulent boundary layer. The AVSL and UPS solutions agree well throughout the shock layer in Fig. 25.

Boundary-layer profiles for the normal-velocity component are shown in Figs. 26–30. Normal velocities are seen to be nearly zero in the laminar boundary layers between $x = 1$ –2 m, Figs. 27–29. UPS predicts slight normal velocities in this region, whereas the LAURA and AVSL solutions remain at zero. This small difference in the UPS profile could be related to

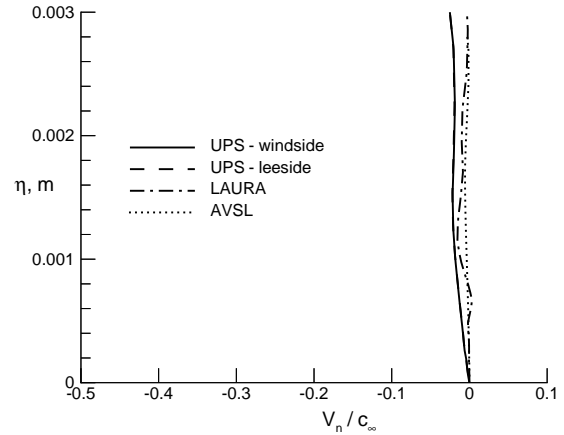


Fig. 28 Boundary-layer normal-velocity profile, $x = 1.5$ m.

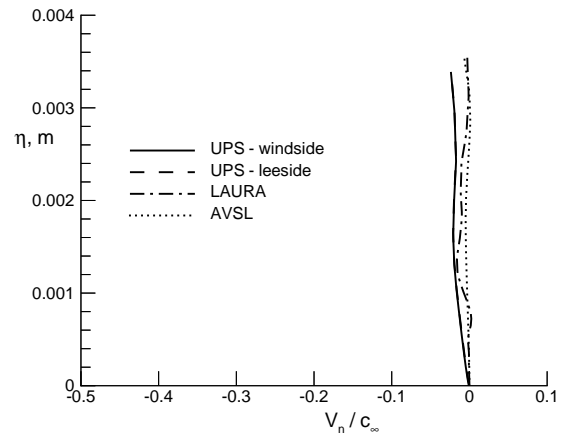


Fig. 29 Boundary-layer normal-velocity profile, $x = 2.0$ m.

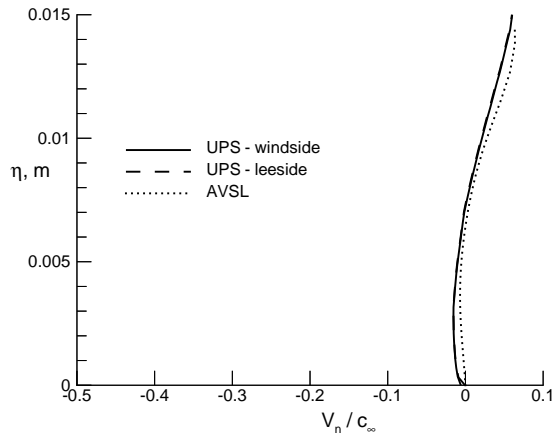


Fig. 30 Boundary-layer normal-velocity profile, $x = 4.0$ m.

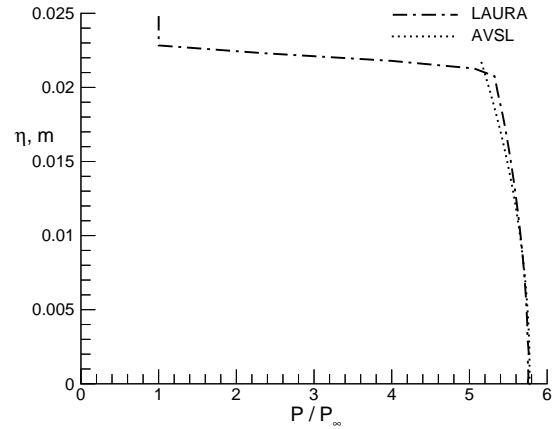


Fig. 32 Shock-layer pressure profile, $x = 1.0$ m.

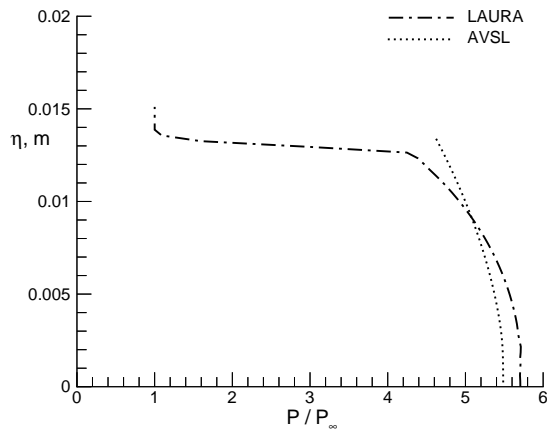


Fig. 31 Shock-layer pressure profile, $x = 0.5$ m.

the imposition of the Vigneron condition on the subsonic portion of the UPS boundary layer.

Further upstream at $x = 0.5$ m, Fig. 26, the normal velocities in the boundary layer deviate linearly from zero, with the UPS magnitudes still larger than either LAURA or AVSL, which agree with each other. These observed non-zero boundary-layer normal-velocity values are indicative of nose-bluntness influence at this station. Still, the magnitudes of the normal-velocity component in the boundary layer are two orders of magnitude smaller than the tangential-velocity components in Fig. 16.

The turbulent normal-velocity profile, Fig. 30, shows an inflection in the profile with positive, out-flowing values in the outer boundary layer. The overall magnitudes, though, remain very near zero.

Pressure profiles

Shock-layer pressure profiles for Cases B and C are presented in Figs. 31–35. The Case A UPS pressures were unavailable for comparison. Excellent agreement through the shock layer between LAURA and AVSL

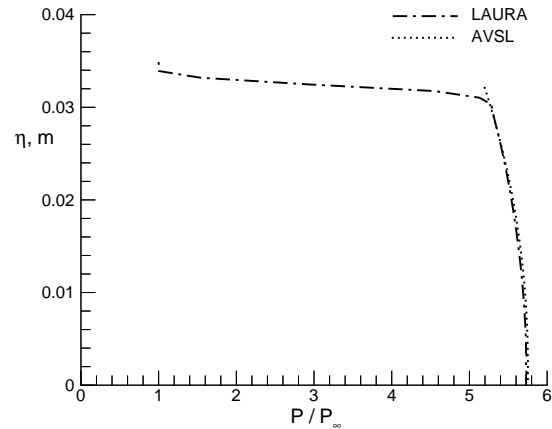


Fig. 33 Shock-layer pressure profile, $x = 1.5$ m.

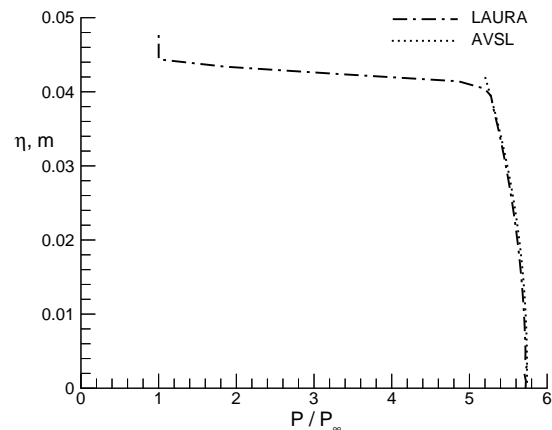


Fig. 34 Shock-layer pressure profile, $x = 2.0$ m.

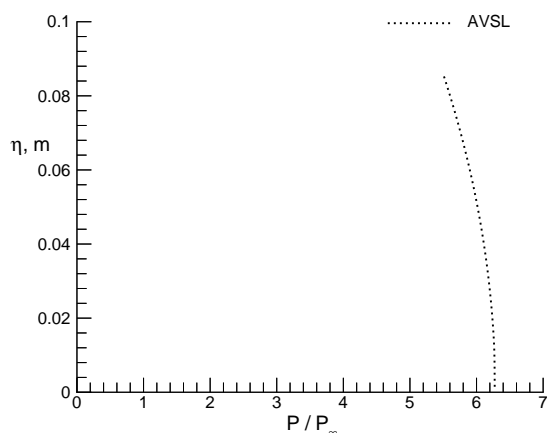


Fig. 35 Shock-layer pressure profile, $x = 4.0$ m.

is seen at the three downstream laminar stations, Figs. 32–34. The surface pressure remains constant along the body in this region at $P/P_\infty = 5.75$.

Closer to the nose, Fig. 31, where nose-bluntness effects are still influential, there are differences between the AVSL and LAURA profiles. The AVSL surface pressure comes in 5 percent lower than the Case B LAURA solution.

The turbulent pressure profile, Fig. 35, retains the same shape as the laminar profiles, but with a 9 percent higher surface pressure. The thicker turbulent boundary layer has pushed the shock further from the body, increasing the shock strength and compression ratio.

Boundary-layer profiles of the pressure are not presented because the pressures remained constant at their edge values for all stations investigated.

Heating

It is noted that surface heat-transfer rates from the Case A solution have been previously presented in Ref. 5. In that report the Case A heating rates are seen to compare very well over the laminar range with data derived from the flight test. Heating agreement between flight and computation is reasonable in the transitional domain and good in the turbulent region toward the aft of the vehicle.

Summary of Results

Three levels of physical modeling were applied to the solution of the Reentry-F flight-vehicle flowfield. Conditions correspond to a flight altitude of 24.4 km (80,000 ft.) at Mach 20. Calculations were performed using equilibrium-air chemistry with algebraic turbulence models. Results are presented in the form of shock-layer and boundary-layer profiles of density, velocity components, and pressure.

Nose-bluntness effects were observed at the $x = 0.5$ m station, 145 nose radii downstream of the vehicle tip, indicated by non-linear shock-layer pro-

files about the conical vehicle. Densities predicted by LAURA were 7 percent larger through the shock layer than given by UPS or AVSL at this station. Further downstream, at $x = 1$ –2 m, very close agreement is seen between the solution sets, particularly with the LAURA and AVSL solutions. Notable exceptions are for the boundary-layer-edge density profiles and the boundary-layer velocities, where the UPS values are 7 percent greater than from LAURA or AVSL.

Pressure profiles show a 5 percent discrepancy between LAURA and AVSL at $x = 0.5$ m, but excellent agreement further downstream. Post-shock pressures are seen to rise by 9 percent after the onset of transition.

The dataset presented herein is intended to provide high-fidelity, state-of-the-art numerical solutions about the Reentry-F flight-test vehicle, which can be utilized in conjunction with the flight-test data to develop and improve transition-prediction models. The development and application of such models is considered an important need for the efficient design of the X-33 and X-34 reusable launch vehicles.

References

- ¹Stainback, P. C., Johnson, C. B., Boney, L. B., and Wicker, K. C., "Comparison of Theoretical Predictions and Heat-Transfer Measurements for a Flight Experiment at Mach 20 (Reentry F)," NASA TM X 2560, 1972.
- ²Gnoffo, P. A., Gupta, R. N., and Shinn, J. L., "Conservation Equations and Physical Models for Hypersonic Air Flows in Thermal and Chemical Nonequilibrium," NASA TP 2867, Feb. 1989.
- ³Cheatwood, F. M. and Thompson, R. A., "The Addition of Algebraic Turbulence Modeling to Program LAURA," NASA TM 107758, April 1993.
- ⁴Buelow, P. E., Tannehill, J. C., Ievalts, J. O., and Lawrence, S. L., "Three-Dimensional, Upwind, Parabolized Navier-Stokes Code for Chemically Reacting Flows," *Journal of Thermophysics and Heat Transfer*, Vol. 5, No. 3, July–Sept. 1991, pp. 274–283.
- ⁵Wood, W. A. and Thompson, R. A., "Combined LAURA-UPS Hypersonic Solution Procedure," NASA TM 107682, March 1993.
- ⁶Wood, W. A., *Combined LAURA-UPS Solution Strategy for Chemically-Reacting Flows*, Master's thesis, University of Washington, Seattle, Washington, June 1994.
- ⁷Wood, W. A., "Dual-Code Solution Strategy for Chemically-Reacting Hypersonic Flows," AIAA Paper 95-0158, Jan. 1995.
- ⁸Wood, W. A., Thompson, R. A., and Eberhardt, S., "Dual-Code Solution Strategy for Hypersonic Flows," *Journal of Spacecraft and Rockets*, Vol. 33, No. 3, May 1996, pp. 449–451.
- ⁹Baldwin, B. S. and Lomax, H., "Thin Layer Approximation and Algebraic Model for Separated Turbulent Flows," AIAA Paper 78-257, January 1978.
- ¹⁰Vigneron, Y. C., Rakich, J. V., and Tannehill, J. C., "Calculation of Supersonic Viscous Flow over Delta Wings with Sharp Subsonic Leading Edges," AIAA Paper 78-1137, Jul. 1978.
- ¹¹Cheatwood, F. M. and DeJarnette, F. R., "An Approximate Viscous Shock Layer Technique for Calculating Chemically Reacting Hypersonic Flows About Blunt-Nosed Bodies," NASA CR 187617, August 1991.

¹²Maslen, S. H., "Inviscid Hypersonic Flow Past Smooth Symmetric Bodies," *AIAA Journal*, Vol. 5, June 1964, pp. 1055–1061.

¹³Srinivasan, S., Tannehill, J. C., and Weilmuenster, K. J., "Simplified Curve Fits for the Thermodynamic Properties of Equilibrium Air," NASA RP 1181, August 1987.

¹⁴Liu, Y. and Vinokur, M., "Equilibrium Gas Flow Computations. I. Accurate and Efficient Calculation of Equilibrium Gas Properties," AIAA Paper 89-1736, Jun. 1989.

¹⁵Cebeci, T. and Smith, A. M. O., "A Finite-Difference Method for Calculating Compressible Laminar and Turbulent Boundary Layers," *Journal of Basic Engineering*, Sep. 1970, pp. 523–535.

¹⁶Hansen, C. F., "Approximations for the Thermodynamic and Transport Properties of High-Temperature Air," NASA TR R-50, 1959.

¹⁷Dhawan, S. and Narashima, R., "Some Properties of Boundary Layer Flow During the Transition from Laminar to Turbulent Motion," *Journal of Fluid Mechanics*, Vol. 3, April 1958.